frontiers | Frontiers in Photonics

TYPE Original Research
PUBLISHED 31 October 2022
DOI 10.3389/fphot.2022.1037473

Upconverting nanoparticles as primary thermometers and power sensors

Joana Costa Martins[1], Artiom Skripka[2], Carlos D. S. Brites[1], Antonio Benayas[3,4], Rute A. S. Ferreira[1], Fiorenzo Vetrone[2] and Luís D. Carlos[1]*

[1]Department of Physics, Phantom-G, CICECO–Aveiro Institute of Materials, University of Aveiro, Campus Universitário de Santiago, Aveiro, Portugal, [2]Centre Énergie, Matériaux et Télécommunications, Institut National de la Recherche Scientifique, Université du Québec, Varennes, QC, Canada, [3]Nanomaterials for Bioimaging Group (nanoBIG), Departamento de Física de Materiales, Facultad de Ciencias, Universidad Autónoma de Madrid, Madrid, Spain, [4]Nanomaterials for Bioimaging Group (nanoBIG), Instituto Ramón y Cajal de Investigación Sanitaria, Madrid, Spain

OPEN ACCESS

EDITED BY
Liang Zhou,
Changchun Institute of Applied Chemistry (CAS), China

REVIEWED BY
Yuhua Wang,
Lanzhou University, China
Xian Chen,
Shenzhen University, China

*CORRESPONDENCE
Luís D. Carlos,
lcarlos@ua.pt

SPECIALTY SECTION
This article was submitted to Light Sources and Luminescent Materials, a section of the journal Frontiers in Photonics

RECEIVED 05 September 2022
ACCEPTED 18 October 2022
PUBLISHED 31 October 2022

CITATION
Martins JC, Skripka A, Brites CDS, Benayas A, Ferreira RAS, Vetrone F and Carlos LD (2022), Upconverting nanoparticles as primary thermometers and power sensors.
Front. Photonics 3:1037473.
doi: 10.3389/fphot.2022.1037473

Luminescence thermometry is a spectroscopic technique for remote temperature detection based on the thermal dependence of the luminescence of phosphors, presenting numerous applications ranging from biosciences to engineering. In this work, we use the Er^{3+} emission of the $NaGdF_4/NaGdF_4:Yb^{3+},Er^{3+}/NaGdF_4$ upconverting nanoparticles upon 980 nm laser excitation to determine simultaneously the absolute temperature and the excitation power density. The Er^{3+} $^2H_{11/2}\rightarrow{}^4I_{15/2}$ and $^4S_{3/2}\rightarrow{}^4I_{15/2}$ emission bands, which are commonly used for thermometric purposes, overlap with the $^2H_{9/2}\rightarrow{}^4I_{13/2}$ emission band, which can lead to erroneous temperature readout. Applying the concept of luminescent primary thermometry to resolve the overlapping Er^{3+} transitions, a dual nanosensor synchronously measuring the temperature and the delivered laser pump power is successfully realized holding promising applications in laser-supported thermal therapies.

KEYWORDS

lanthanides (III), upconversion nanoparticles (UCNPs), luminescent nanothermometer, NIR radiation sensor, bioimaging

Introduction

Luminescent nanothermometry exploits the temperature-dependent emission properties of luminescent nanoprobes, e.g., quantum dots, organic dyes, polymers, DNA or protein conjugated systems, transition-metal-based materials, or trivalent lanthanide ion (Ln^{3+})-doped materials (Brites et al., 2012; Jaque and Vetrone, 2012; Brites et al., 2016). The latter systems feature unique characteristics, such as high photostability, narrow bandwidth, and efficient room-temperature emission, which make them suitable for different applications, particularly bioimaging-related ones (Jaque et al., 2014; Zhou et al., 2015; Brites et al., 2016; Dramicanin, 2018; Brites et al., 2019a). Ln^{3+} ions work in the spectral ranges where the biological tissue has minimal absorption and negligible autofluorescence, designated as biological imaging windows. Therefore, luminescent thermometers based on Ln^{3+}-doped nanomaterials have been widely employed in intracellular measurements (Debasu et al., 2020; Piñol et al., 2020; Dantelle et al., 2021; Di et al., 2021; Kim et al., 2021; Dos Santos et al., 2022) and tumor temperature mapping during thermal therapies (Jaque et al., 2014; Carrasco et al., 2015; Zhu et al., 2016, 2018).

The most common approach to infer absolute temperature is based on the intensity ratio of two distinct transitions - ratiometric luminescence thermometry (Brites et al., 2016). In the last few years, primary thermometers based on luminescent nanoprobes have been studied which take advantage of the temperature-dependent intensity ratio of the two thermally coupled Er^{3+} levels, $^2H_{11/2}$ and $^4S_{3/2}$ (Balabhadra et al., 2017; Bastos et al., 2019; Brites et al., 2019b; Martínez et al., 2019; Borges et al., 2021; Martins et al., 2021; Dos Santos et al., 2022). A primary thermometer is characterized by a well-established emitting state population equation that follows Boltzmann statistics. Recently, a few works have drawn attention to the impact of the $^2H_{9/2}\rightarrow{}^4I_{13/2}$ emission band in temperature determination using Er^{3+} emission (Martins et al., 2021; Rühl et al., 2021; Van Swieten et al., 2021; Xia et al., 2021). Upon near-infrared (NIR) excitation, the $^2H_{9/2}$ manifold of Er^{3+} is populated through a three-photon upconversion process (Cho et al., 2017). Emission of the $^2H_{9/2}\rightarrow{}^4I_{13/2}$ transition overlaps with the $^4S_{3/2}\rightarrow{}^4I_{15/2}$ one, which can lead to total intensity overestimation when $^2H_{9/2}\rightarrow{}^4I_{13/2}$ contribution is overlooked, and its contribution increases with the excitation power density (P_D) (Zhou et al., 2013; Berry and May, 2015; Yuan et al., 2018, 2019; Rühl et al., 2021; Xia et al., 2021). This complicates accurate temperature readout but provides an opportunity to explore NIR P_D optical readout, as demonstrated herein. To the best of our knowledge, only one luminescent excitation density ratiometric sensor for the visible spectral range was reported by (Marciniak et al. (2022)). There, the intensity ratio of $^4T_{2(g)}\rightarrow{}^4A_{2(g)}$ and $^2E_{(g)}\rightarrow{}^4A_{2(g)}$ transitions of $GdAl_3(BO_3)_4$:Cr^{3+} nanoparticles was used to measure the excitation power density at 445 nm and 532 nm. The authors designed the nanoparticles to enhance the probability of nonradiative processes to achieve an efficient radiation-to-heat conversion. The designed material reached temperatures as high as 143°C, even at low excitation power density. According to the excitation power density, the heat generated in the system leads to the thermalization of the $^4T_{2(g)}$ state inducing a change in the intensity ratio (Marciniak et al., 2022), and thus, the working principle of this Cr^{3+} ratiometric laser power meter is, in fact, temperature related.

The simultaneous measurement of temperature and incident P_D is critical for optimizing photon-based therapies, such as photothermal therapy (Jaque et al., 2014; Yang et al., 2017) and photobiomodulation (PBM) (Freitas and Hamblin, 2016), and preventing the surrounding tissue from overheating and deleterious damage (Shen et al., 2020). Photothermal therapy uses light to generate heat from plasmonic or dielectric nanoparticles (Jaque et al., 2014), whereas PBM involves the use of a low-powered light source (lasers and LEDs) within the red and NIR wavelength range (~600–1,000 nm) to stimulate or inhibit cellular and biological processes (Freitas and Hamblin, 2016). In PBM applications, where the low-powered excitation source does not induce an evident temperature rise, the P_D quantization of the delivered light to the target could contribute to standardization, improving the reliability and reproducibility of the technique (Wang and Dong, 2020).

In this work, we study the thermometric features of $NaGdF_4$/$NaGdF_4$:Yb^{3+},Er^{3+}/$NaGdF_4$ upconverting nanoparticles upon 980 nm laser excitation and show how they work as a primary luminescent thermometer once the decoupling procedure is applied to resolve the overlapping $^2H_{9/2}\rightarrow{}^4I_{13/2}$ and $^4S_{3/2}\rightarrow{}^4I_{15/2}$ emission bands. The passive-core/active-shell/passive-shell architecture of nanoparticles was chosen to promote Er^{3+} upconversion emission from the $^2H_{9/2}$ excited state, through reduced energy migration and enhanced energy transfer upconversion (Chen et al., 2016; Wang, 2019). Taking advantage of the P_D-dependent $^2H_{9/2}\rightarrow{}^4I_{13/2}$ emission intensity, we characterize a ratiometric NIR radiation sensor. Thus, we have developed a versatile system capable of sensing both the local absolute temperature and the P_D delivered to the target using luminescence with future potential applications in PBM treatments or other laser-based thermal therapies.

Besides being a NIR radiation sensor, which is the radiation commonly used in biological applications, the monodisperse in size $NaGdF_4$/$NaGdF_4$:Yb^{3+},Er^{3+}/$NaGdF_4$ nanoparticles can be patterned on various substrates as well as dispersed in different colloidal mixtures. Moreover, the intensity of the selected transitions to sense the delivered laser pump power are thermal independent, enabling the synchronous measurement of the temperature and P_D.

Materials and methods

Materials synthesis

$NaGdF_4$/$NaGdF_4$: 2 mol% Er^{3+}, 20 mol% Yb^{3+}/$NaGdF_4$ lanthanide-doped nanoparticles (Figure 1), were prepared by hot-injection thermal decomposition (Boyer et al., 2006; Skripka et al., 2020).

To synthesize the core, an initial mixture of 12.5 mL each of OA and ODE was prepared in a 100 mL three-neck round bottom flask (Solution A). Aside, 2.5 mmol of Na-TFA were added to the 2.5 mmol of dried Gd-TFA precursor together with 7.5 mL each of OA and ODE (Solution B). Both solutions A and B were degassed at 150°C under vacuum with magnetic stirring for 30 min. After degassing, solution A was placed under an Ar atmosphere and the temperature was raised to 315°C. Solution B was then injected into the reaction vessel containing solution A

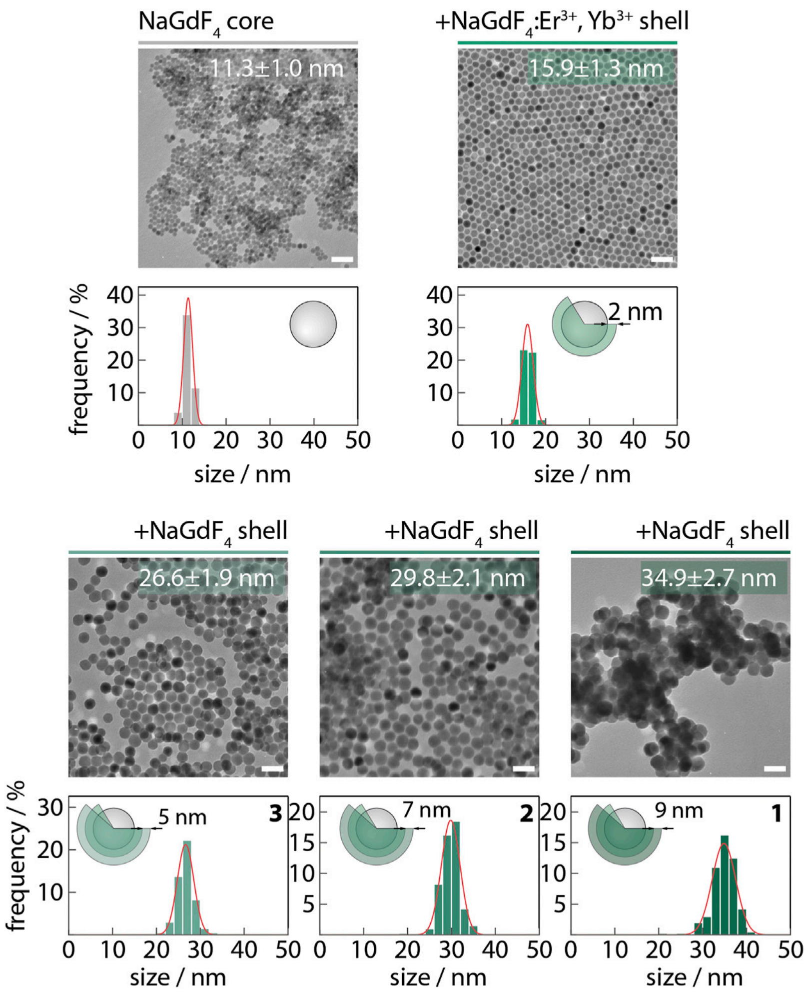

FIGURE 1
Representative TEM images of Er^{3+}-doped nanothermometers and their respective size distributions. The thickness of the outer $NaGdF_4$ shell is represented in the scheme. The nanoparticles used in this work, 1, 2, and 3, are represented in the lower panel. The solid lines are the best fits to the experimental data using Gaussian distributions ($r^2 > 0.99$). The scale bars correspond to 50 nm.

with a syringe and pump system at a 1.3 mL/min injection rate. The mixture was left at 315°C under vigorous stirring for 60 min. After cooling to room temperature, the as-synthesized cores (11.3 nm) were stored in a Falcon centrifuge tube under Ar for further synthesis steps. The core/shell $NaGdF_4/NaGdF_4{:}Er^{3+}$, Yb^{3+} nanoparticles were prepared by a subsequent shelling of the 2.5 mmol of core nanoparticles (solution A). Separately, solution B contained 3.5 mmol of Na-TFA precursors and 3.5 mmol of Gd,Yb,Er-TFA (2.73 mmol + 0.7 mmol + 0.07 mmol) together with 7.5 mL each of OA and ODE. Both solutions were degassed at 150°C under vacuum with magnetic stirring for 30 min. After degassing, solution A was placed under an Ar atmosphere and the temperature was raised to 315°C. Solution B was then injected at a 1 mL/min rate into solution A and left to react for 90 min. After, 15 mL of the reaction mixture containing core/shell1 nanoparticles (15.9 nm) was aliquoted for sampling. The core/shell/shell $NaGdF_4/NaGdF_4{:}Er^{3+}$, $Yb^{3+}/NaGdF_4$ with various thicknesses of the most-outer shell were prepared by subsequent injection of shelling precursors into the reaction. 8 mmol each of Na-TFA and Gd-TFA were dissolved and degassed in a mixture of 10 mL each of OA and ODE (solution C). Half (10 mL) of solution C was injected at 1 ml/min into the reaction flask and kept at a pre-set 315°C temperature for 60 min, 10 mL of the reaction mixture was aliquoted from the flask before injecting the rest of the solution C. After 60 min, 10 mL were aliquoted from the reaction flask, obtaining core/shell/shell RENPs with a 5.4 nm thick outer shell. Another 8 mmol each of Na-TFA and Gd-TFA were dissolved and degassed in a mixture of 10 mL each of OA and ODE (solution D) and injected (10 mL) into the reaction flask. After 60 min, 10 mL were aliquoted from the reaction obtaining core/shell/shell RENPs with 7.0 nm thick outer shell.

The remaining 10 mL of the solution D were then injected into the reaction mixture and allowed to react for 60 min, yielding core/shell/shell RENPs with a 9.5 nm thick outer shell. The mixture was cooled to room temperature, and core-only, core/shell, and core/shell/shell RENPs were precipitated with ethanol and washed three times with hexane/ethanol (1/4 v/v), followed by centrifugation (5400 RCF). Samples containing $NaGdF_4$/$NaGdF_4$:Er^{3+},Yb^{3+}/$NaGdF_4$ RENPs with outer shell thicknesses of 9.5, 7.0, and 5.4 nm dispersed in water (nanofluids) were designated as **1**, **2** and **3**, respectively.

Structural characterization methods

The morphology and size distribution of the core-only and core/shell UCNPs were investigated by transmission electron microscopy (TEM, Philips Tecnai 12). The particle size was determined from TEM images using ImageJ software with a minimum set size of 200 individual UCNPs per sample. The crystallinity and phase of all the UCNPs were determined *via* X-ray powder diffraction (XRD) analysis with a Bruker D8 Advance Diffractometer (USA) using Cu K_α radiation.

Power density and temperature-dependent photoluminescence measurements

The **1**, **2**, and **3** nanofluids were placed in a quartz cuvette (114F–10–40, Hellma Analytics) and were excited with a pulsed laser (BrixX 980–1000 HD, Omicron Laser) at a frequency of 1.5 MHz, to get an essentially continuous wave irradiation mode. The laser was focused through an optical lens of 7.5 cm focal distance (LA1145, Thorlabs) to enhance the power density (P_D) that ranges from 29.0 ± 0.1 to 138.8 ± 0.7 W cm^{-2}, estimated as previously reported (Caixeta et al., 2020). The emission light was guided through an optical fiber (P600-1-UV-VIS, Ocean Insight) and the laser contribution was cut out with a short-pass optical filter (FESH0750, Thorlabs). The emission spectra were recorded by a portable spectrometer (MAYA Pro 2000; Ocean Insight) using an acquisition window between 15–75 s (a total of 150 measurements with integration time ranging from 0.1 to 0.5 s), adjusting the acquisition conditions to obtain a similar signal-to-noise (SNR) ratio at the different excitation P_D. The spectrometer uses reference and dark measurements to correct the instrument response.

The quartz cuvette was placed in thermal contact with a homemade temperature controller containing a Peltier system and a thermocouple (K-type, 0.1 K accuracy) that was immersed near the laser spot, but away from the light path to monitor and measure the temperature (T) of the nanofluid. We set the temperature controller at a fixed temperature and turned on the excitation laser at a fixed P_D inducing an additional temperature increment. After the nanofluid reaches thermal equilibrium (t > 350 s) the emission spectra and thermocouple reading are recorded. This process was repeated for P_D ranging from 19.0 to 138.8 W cm^{-2} and for different set temperatures (297.6–315.3 K). At the lowest temperature used (room temperature), the temperature controller was kept off.

Sensing parameters determination

Before the calculus of the thermometric parameter (Δ) and NIR radiation sensing parameter (Δ_{NIR}), a spectral deconvolution procedure based on a previously reported work (Martins et al., 2021) was applied to the emission spectra to decouple the overlapping transitions, $^2H_{9/2}\rightarrow^4I_{13/2}$ and $^4S_{3/2}\rightarrow^4I_{15/2}$, using a routine in MatLab© software. The routine starts with a baseline subtraction to remove the remaining spectrometer electric noise, followed by the conversion of the signal of each emission spectrum from wavelength to energy units by applying the Jacobian transformation (Mooney and Kambhampati, 2013). Then, the [17,500, 19,500] cm^{-1} spectral region was fitted using a multiparametric Gaussian function. Good fits to the experimental data (R^2 > 0.99) were obtained with a minimum number of Gaussian functions equal to 10 (two, four, and four Gaussian functions described the $^2H_{9/2}\rightarrow^4I_{13/2}$, $^4S_{3/2}\rightarrow^4I_{15/2}$, and $^2H_{11/2}\rightarrow^4I_{15/2}$ transitions, respectively). The intensities of the transitions were estimated by the sum of the fitted areas of the respectively assigned Gaussian functions. The parameters Δ and Δ_{NIR} are computed for the 150 recorded emission spectra for each P_D and T, where Δ, Δ_{NIR} and the respective uncertainties ($\delta\Delta$ and $\delta\Delta_{NIR}$, respectively) are extracted from the corresponding histograms (mean ± standard deviation). To evaluate the performance of the luminescent thermometer, the relative thermal sensitivity, S_r, and the minimum temperature uncertainty, δT, are determined, as follows (Brites et al., 2016):

$$\boldsymbol{S_r = \frac{1}{\Delta}\left|\frac{\partial\Delta}{\partial T}\right| = \frac{\Delta E}{k_B T^2}} \tag{1}$$

and

$$\boldsymbol{\delta T = \frac{1}{S_r}\frac{\delta\Delta}{\Delta}} \tag{2}$$

where $\delta\Delta$ is the uncertainty in the determination of Δ. S_r, which represents the relative Δ change per temperature degree, is an intrinsic property of the nanothermometer material (Brites et al., 2016).

Results and discussion

Primary thermometer

Figure 2 illustrates the emission spectra of **1** for selected P_D values exhibiting Er^{3+} transitions in the green, $^2H_{11/2}\rightarrow^4I_{15/2}$ and

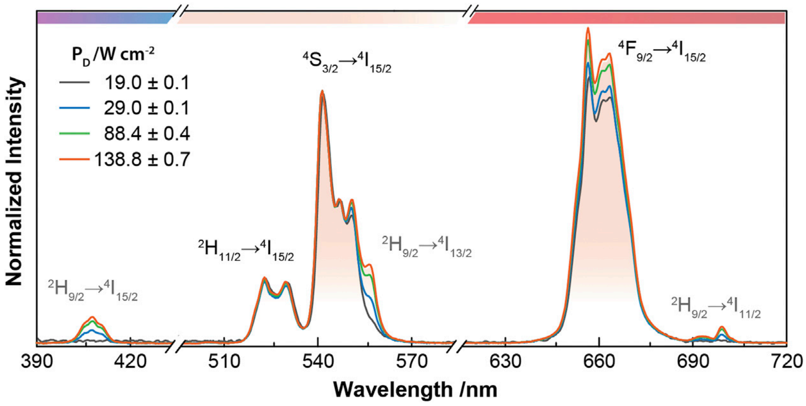

FIGURE 2
Normalized upconversion emission spectra of **1** as a function of P_D measured at room temperature. The spectra are normalized to the $^4S_{3/2}\rightarrow{}^4I_{15/2}$ transition.

$^4S_{3/2}\rightarrow{}^4I_{15/2,}$ and red spectral regions, $^4F_{9/2}\rightarrow{}^4I_{15/2}$ (Auzel, 2004). Evidence of the $^2H_{9/2}$ level population can be found in the transitions in the blue, $^2H_{9/2}\rightarrow{}^4I_{15/2}$, and red spectral region, $^2H_{9/2}\rightarrow{}^4I_{11/2}$. Additionally, the band overlapping with the $^4S_{3/2}\rightarrow{}^4I_{15/2}$ emission corresponds to the $^2H_{9/2}\rightarrow{}^4I_{13/2}$ transition, whose intensity shows similar power-dependence to the $^2H_{9/2}\rightarrow{}^4I_{11/2,15/2}$ transitions (Berry and May, 2015; Cho et al., 2017). Since the population of the $^2H_{9/2}$ level is reached *via* a three-photon upconversion process, the intensity of radiative transitions from the $^2H_{9/2}$ level shows a different behavior with P_D than the $^2H_{11/2}\rightarrow{}^4I_{15/2}$ and $^4S_{3/2}\rightarrow{}^4I_{15/2}$ transitions (Renero-Lecuna et al., 2011; Zhou et al., 2013; Cho et al., 2017). A similar trend is observed for $^4F_{9/2}\rightarrow{}^4I_{15/2}$, where, at higher P_D, the upper levels, $^2H_{11/2}$ and $^4S_{3/2}$ become saturated favoring the population of the $^4F_{9/2}$ emitting level due to nonradiative relaxations upon the local heating induced by the laser excitation (Kraft et al., 2018; Maturi et al., 2021). The emission spectra of **2** and **3** measured at the lowest measured P_D display analogous emission spectra of **1**, except for the worse SNR (Supplementary Figure S1). As the shell gets thicker, the luminescence quenching effects are reduced (Pini et al., 2022; Shi et al., 2022) leading to higher SNR and advantageously decreased temperature uncertainty. As initially proposed by some of us (Brites et al., 2016), and experimentally implemented by others (Van Swieten et al., 2021), the temperature uncertainty increases as the SNR degrades. The value of the relative thermal uncertainty for **1** is about 78% and 49% smaller than those obtained for **2** and **3**, respectively, in similar excitation and collection conditions (Supplementary Figure S2). For this reason, **1** was the chosen nanofluid to perform the onward photoluminescent measurements.

The Er^{3+} emission in the green spectral region, namely the $^2H_{11/2}\rightarrow{}^4I_{15/2}$ and $^4S_{3/2}\rightarrow{}^4I_{15/2}$ transitions, have been widely explored for thermometric purposes in light upconverting nanoparticles since its first report in 2010 (Vetrone et al., 2010). The intensity ratio of these two transitions is temperature-dependent according to Boltzmann statistics, which governs the population distribution between the two thermally coupled levels, $^2H_{11/2}$ and $^4S_{3/2}$. Recently, these thermometers have been explored as primary luminescent thermometers, in which the intensity ratio between $^2H_{11/2}\rightarrow{}^4I_{15/2}$ (I_H) and $^4S_{3/2}\rightarrow{}^4I_{15/2}$ (I_S) emissions bands are directly related to the absolute temperature, T, through a well-established equation of state population (Balabhadra et al., 2017; Brites et al., 2019b; Martínez et al., 2019; Back et al., 2020):

$$\frac{1}{T}=\frac{1}{T_0}-\frac{k_B}{\Delta E}\ln\frac{\Delta}{\Delta_0} \tag{3}$$

where k_B is the Boltzmann constant, ΔE is the energy gap between the barycenters of the $^2H_{11/2}$ and $^4S_{3/2}$ levels, and $\Delta = I_H/I_S$ the thermometric parameter with Δ_0 being the value at the temperature T_0 (see Supporting Information for the calculus of ΔE and Δ_0).

Regarding temperature determination through the intensity ratio between the $^2H_{11/2}\rightarrow{}^4I_{15/2}$ and $^4S_{3/2}\rightarrow{}^4I_{15/2}$, a few works have been raising awareness of the impact of the $^2H_{9/2}\rightarrow{}^4I_{13/2}$ transition and how it can affect the temperature measurements, especially when a laser P_D variation is imposed (Martins et al., 2021; Rühl et al., 2021; Van Swieten et al., 2021; Xia et al., 2021).

Figure 3A shows the temperature dependence of the emission spectra of **1** excited at selected P_D values and set temperatures (297.6, 305.3, and 315.3 K). Since the $^2H_{9/2}\rightarrow{}^4I_{13/2}$ and $^4S_{3/2}\rightarrow{}^4I_{15/2}$ emission bands are overlapped, and Equation 3 accounts only for the emissions of the two thermally coupled levels ($^2H_{11/2}$ and $^4S_{3/2}$), the emission bands must be decoupled to correctly estimate I_S. Thus, a spectral deconvolution, consisting of a multiparametric Gaussian fit, is applied and the $^2H_{9/2}\rightarrow{}^4I_{13/2}$ (I_X), $^4S_{3/2}\rightarrow{}^4I_{15/2}$ (I_S), and $^2H_{11/2}\rightarrow{}^4I_{15/2}$ (I_H) transitions

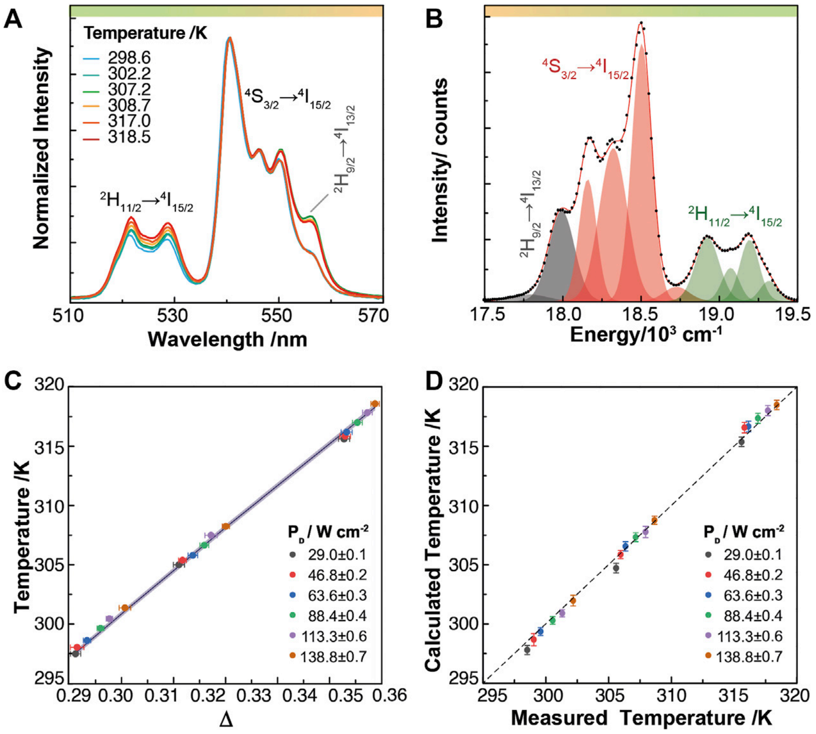

FIGURE 3
(A) Temperature-dependent upconversion emission spectra of **1** excited at 29.0, 88.4 and 138.8 W cm^{-2}. **(B)** Spectral Gaussian deconvolution of the emission spectrum measured at 302.2 K and 138.8 W cm^{-2}. The black dots and the red line represent the experimental data and the fit envelope of the spectrum, respectively. The shadowed areas correspond to the Gaussian functions assigned to the $^2H_{9/2}\rightarrow{}^4I_{13/2}$ (black), $^4S_{3/2}\rightarrow{}^4I_{15/2}$ (red), and $^2H_{11/2}\rightarrow{}^4I_{15/2}$ (green) transitions. **(C)** Temperature dependence of the experimental Δ values determined under laser excitation at different P_D values. The horizontal error bars represent the error in the measured thermometric parameters (Supplementary Equation S1 in Supporting Information). The line is the theoretical prediction of the temperature (Equation 3) and the shadowed area is the corresponding uncertainty (Supplementary Equation S2 in Supporting Information). **(D)** Measured temperature (thermocouple reading) *versus* calculated temperature (Equation 3) under laser excitation at different P_D values. The vertical error bars correspond to the shadowed area of the line represented in C. The thermocouple accuracy is 0.1 K.

intensities are estimated by the sum of the fitted areas of the assigned Gaussians to the respective transitions (Figure 3B) (see further details in Materials and Methods).

We observe that the calculated Δ are within the theoretical prediction by Equation 3, independently of the excitation P_D values (Figure 3C). Δ is converted to absolute temperature substituting the corresponding parameters (Δ_0, T_0, *and* ΔE, Supplementary Figures S3, S4 and Supporting Information for further details) in Equation 3. The calculated temperatures are in excellent agreement with the experimental ones, demonstrating that **1** works as a primary luminescent thermometer. Besides guaranteeing reliable temperature measurements, the primary luminescent thermometer demonstrated the correct decoupling of both transitions ($^2H_{9/2}\rightarrow{}^4I_{13/2}$ and $^4S_{3/2}\rightarrow{}^4I_{15/2}$) in the P_D range of 29.0–138.8 W cm^{-2}. Moreover, it is experimentally verified, for the first time, the independence of the primary luminescent thermometer on excitation P_D (Figure 3D).

The S_r of **1** is within the commonly reported range for Er^{3+} based nanothermometers (~0.2–1 %K^{-1}), since ΔE is not considerably affected by its host matrix (Figure 4A). Besides the material, δT also depends on the SNR of the measurement, which means this figure of merit is strongly affected by the type and performance of the detector and experimental conditions, such as luminescent material quantity, acquisition time, and background noise, thus precluding a fair comparison with reported values in the literature (Brites et al., 2016; Van Swieten et al., 2022). Nevertheless, in this work, the minimum δT is 0.3 K at 297.5 K (Figure 4B), which is above 0.2 K, the minimum possible value, as reported by (Van Swieten et al. (2022)).

NIR radiation sensor

The high sensitivity of the $^2H_{9/2}\rightarrow{}^4I_{13/2}$ intensity to P_D values led us to further study these luminescent nanoparticles as a potential NIR radiation sensor. Since emission intensities depend on a multitude of parameters (e.g., temperature,

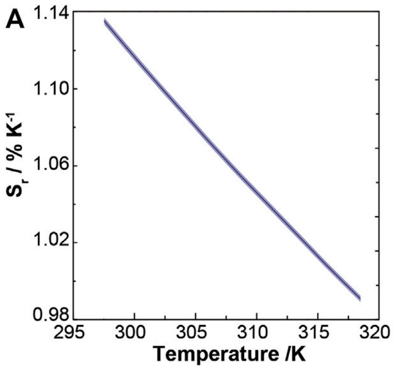

FIGURE 4
(A) Relative thermal sensitivity and **(B)** temperature uncertainty of **1.** The corresponding uncertainties (Supplementary Equations S3, S4 in Supporting Information) are represented by the shadowed areas.

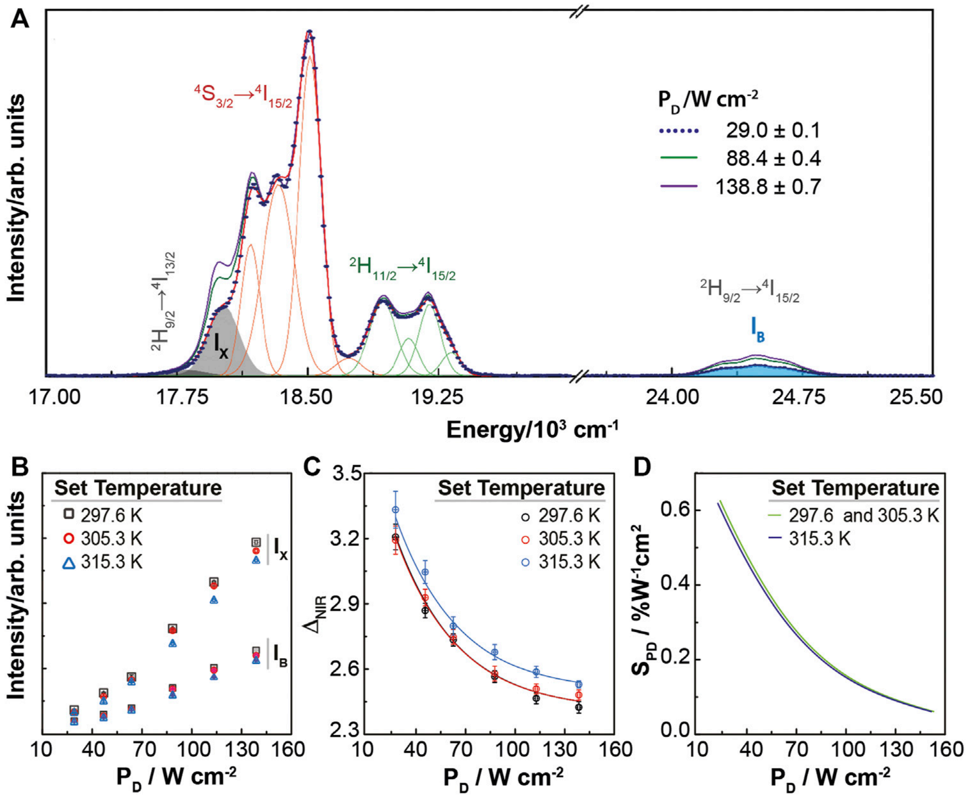

FIGURE 5
(A) Upconversion emission spectra of **1** for selected P_D values (297.6 K set temperature) depicting the spectral Gaussian deconvolution (green and red lines ascribed to $^2H_{11/2}\rightarrow^4I_{15/2}$ and $^4S_{3/2}\rightarrow^4I_{15/2}$ transitions) and the I_X and I_B areas for 29.0 W cm^{-2} (grey and blue shadowed regions). Dependence on P_D of **(B)** I_X and I_B and **(C)** Δ_{NIR}, for the indicated set temperatures. The lines correspond to the best fits to the experimental data using Equation 4 ($r^2 > 0.98$). **(D)** Corresponding relative sensitivity to P_D of the NIR sensor based on **1**.

power density, sensor concentration, material inhomogeneities and optoelectronic drifts in detection) (Brites et al., 2012), we define the NIR radiation sensing parameter as an intensity ratio, $\Delta_{\mathrm{NIR}} = I_X/I_B$, calculated using the emission intensity of the $^2H_{9/2}\rightarrow^4I_{15/2}$ (I_B) and $^2H_{9/2}\rightarrow^4I_{13/2}$ (I_X) transitions (Figure 5A).

The power-dependence of I_X and I_B is different (Figure 5B) resulting in a decreasing Δ_{NIR} with P_D values (Figure 5C). Changing P_D for the set temperatures 297.6 and 305.3 K, Δ_{NIR} is the same within the uncertainty, while at a higher set temperature (315.3 K) an offset in Δ_{NIR} values is observed. Therefore, we characterize **1** as a NIR sensor with a specific calibration according to the working temperature ranges (298.5–308.7 K and 315.6–318.5 K, Figure 3D).

To determine a working calibration curve that describes Δ_{NIR} variation in the measured P_D range, we assume a generic and empirical equation that better fits the experimental data since we lack a theoretical model. As the behavior observed for Δ_{NIR} variation is similar in both temperature ranges and only differs by an offset, the following function:

$$\Delta_{NIR} = A\exp\left(-\frac{P_D}{t}\right) + y_0 \tag{4}$$

was fitted to both experimental datasets with A and t parameters shared between the two fits while y_0 was kept free (Figure 5C). The resulting fitting parameters are $A = 1.74 \pm 0.09$, $t = 37 \pm 1$ W cm^{-2}, $y_{01} = 2.41 \pm 0.01$ and $y_{02} = 2.50 \pm 0.01$, corresponding to y_0 in the 298.5–308.7 K and 315.6–318.5 K ranges, respectively. Inspired by the definition of the relative thermal sensitivity of a thermometer (Equation 1), we define the relative sensitivity to P_D, S_{PD}, as a figure of merit to characterize the NIR sensor:

$$S_{PD} = \frac{1}{\Delta_{NIR}}\left|\frac{\partial \Delta_{NIR}}{\partial P_D}\right| = \left|\frac{-\Delta_{NIR} + y_0}{t\Delta_{NIR}}\right| \tag{5}$$

yielding a maximum value of 0.5% W^{-1}·cm^2 at 29.0 W cm^{-2} (Figure 5D), which is higher than the value reported for the luminescent Cr^{3+}-based ratiometric radiation sensor, 0.07% W^{-1} cm^2, (Marciniak et al., 2022).

Conclusion

The Er^{3+} emission of the $NaGdF_4/NaGdF_4{:}Yb^{3+},Er^{3+}/NaGdF_4$ upconverting nanoparticles upon 980 nm laser excitation was used to develop a luminescent dual nanosensor synchronously measuring the temperature and the delivered laser pump power. Both sensing capabilities use the same simple instrumentation, providing reliable temperature readout through the concept of luminescent primary thermometry to resolve the overlapping of the $^2H_{9/2}\rightarrow 4I_{13/2}$ and $^4S_{3/2}\rightarrow 4I_{15/2}$ emissions. Moreover, the measurements are independent and there are no temperature-P_D crossover effects in the studied temperature. This dual-sensor shows potential for laser-assisted biomedical applications, such as *in-vivo* real-time temperature monitoring during photothermal therapies, where human exposure to NIR laser radiation must be strictly controlled to avoid healthy tissue damage and, thus, ensuring a safe and efficient therapy implementation. In context, under the International Commission on Non-Ionizing Radiation Protection (ICNIRP) guidelines, skin exposure to 980 nm laser radiation is limited to 0.73 W cm^{-2} for exposures times of 10 s to 8 h (Ziegelberger, 2013). However, for deliberate exposure as part of medical treatment, these radiation limits vary according to the procedure and instrumentation regulated by U.S. Food and Drug Administration (FDA) (FDA, 2020), and thus demand for flexible in situ power verification.

Data availability statement

The raw data supporting the conclusions of this article will be made available by the authors, without undue reservation.

Author contributions

JM: Photoluminescence characterization, draft and figures preparation. AS, AB, and FV: Conceptualization, supervising the synthesis of the particles, data curation, and validation of the synthesis and structural characterization of the prepared particles. CB, RF, and LC: Conceptualization of the luminescent thermometry and delivered laser power density sensor, methodology of photoluminescence measurements, data curation on photoluminescence, validation, writing, reviewing, and editing on the final manuscript and figures.

Funding

This work was developed within the scope of the project CICECO-Aveiro Institute of Materials, UIDB/50011/2020, UIDP/50011/2020 and LA/P/0006/2020, financed by national funds through the FCT/MEC (PIDDAC).

Acknowledgments

JM and AS are grateful to FCT (SFRH/BD/139710/2018) and Fonds de Recherche du Québec-Nature et technologies (FRQNT) for financial support in the form of scholarships for doctoral studies, respectively. AB acknowledges funding support from Comunidad de Madrid through TALENTO grant ref. 2019-T1/IND-14014.

Conflict of interest

Publisher's note

Supplementary material

The Supplementary Material for this article can be found online at: https://www.frontiersin.org/articles/10.3389/fphot.2022.1037473/full#supplementary-material

References

Auzel, F. (2004). Upconversion and anti-Stokes processes with *f* and *d* ions in solids. *Chem. Rev.* 104, 139–174. doi:10.1021/cr020357g

Back, M., Casagrande, E., Brondin, C. A., Ambrosi, E., Cristofori, D., Ueda, J., et al. (2020). Lanthanide-doped $Bi_2SiO_5@SiO_2$ core-shell upconverting nanoparticles for stable ratiometric optical thermometry. *ACS Appl. Nano Mat.* 3, 2594–2604. doi:10.1021/acsanm.0c00003

Balabhadra, S., Debasu, M. L., Brites, C. D. S., Ferreira, R. A. S., and Carlos, L. D. (2017). Upconverting nanoparticles working as primary thermometers in different media. *J. Phys. Chem. C* 121, 13962–13968. doi:10.1021/acs.jpcc.7b04827

Bastos, A. R. N., Brites, C. D. S., Rojas-Gutierrez, P. A., DeWolf, C., Ferreira, R. A. S., Capobianco, J. A., et al. (2019). Thermal properties of lipid bilayers determined using upconversion nanothermometry. *Adv. Funct. Mat.* 29, 1905474–1905510. doi:10.1002/adfm.201905474

Berry, M. T., and May, P. S. (2015). Disputed mechanism for NIR-to-red upconversion luminescence in $NaYF_4$:Yb^{3+}, Er^{3+}. *J. Phys. Chem. A* 119, 9805–9811. doi:10.1021/acs.jpca.5b08324

Borges, F. H., Martins, J. C., Caixeta, F. J., Pereira, R. R., Carlos, L. D., Ferreira, R. A. S., et al. (2021). Primary thermometers based on sol–gel upconverting Er^{3+}/Yb^{3+} Co-doped yttrium tantalates with high upconversion quantum yield and emission color tunability. *J. Sol-Gel Sci. Technol.* 102, 249–263. doi:10.1007/s10971-021-05673-0

Boyer, J.-C., Vetrone, F., Cuccia, L. A., and Capobianco, J. A. (2006). Synthesis of colloidal upconverting $NaYF_4$ nanocrystals doped with Er^{3+}, Yb^{3+} and Tm^{3+}, Yb^{3+} via thermal decomposition of lanthanide trifluoroacetate precursors. *J. Am. Chem. Soc.* 128, 7444–7445. doi:10.1021/ja061848b

Brites, C. D. S., Balabhadra, S., and Carlos, L. D. (2019a). Lanthanide-based thermometers: At the cutting-edge of luminescence thermometry. *Adv. Opt. Mat.* 7, 1801239–1801330. doi:10.1002/adom.201801239

Brites, C. D. S., Lima, P. P., Silva, N. J. O., Millán, A., Amaral, V. S., Palacio, F., et al. (2012). Thermometry at the nanoscale. *Nanoscale* 4, 4799–4829. doi:10.1039/c2nr30663h

Brites, C. D. S., Martínez, E. D., Urbano, R. R., Rettori, C., and Carlos, L. D. (2019b). Self-calibrated double luminescent thermometers through upconverting nanoparticles. *Front. Chem.* 7, 267–310. doi:10.3389/fchem.2019.00267

Brites, C. D. S., Millán, A., and Carlos, L. D. (2016). "Lanthanides in luminescent thermometry," in *Handbook on the physics and Chemistry of rare earths*. Editors J-C. Bünzli and V. K. Pecharsky (Netherland: Elsevier, B.V), 339–427. doi:10.1016/bs.hpcre.2016.03.005

Caixeta, F. J., Bastos, A. R. N., Botas, A. M. P., Rosa, L. S., Souza, V. S., Borges, F. H., et al. (2020). High-quantum-yield upconverting Er^{3+}/Yb^{3+}-organic-inorganic hybrid dual coatings for real-time temperature sensing and photothermal conversion. *J. Phys. Chem. C* 124, 19892–19903. doi:10.1021/acs.jpcc.0c03874

Carrasco, E., Del Rosal, B., Sanz-Rodríguez, F., De La Fuente, Á. J., Gonzalez, P. H., Rocha, U., et al. (2015). Intratumoral thermal reading during photo-thermal therapy by multifunctional fluorescent nanoparticles. *Adv. Funct. Mat.* 25, 615–626. doi:10.1002/adfm.201403653

Chen, X., Jin, L., Kong, W., Sun, T., Zhang, W., Liu, X., et al. (2016). Confining energy migration in upconversion nanoparticles towards deep ultraviolet lasing. *Nat. Commun.* 7, 10304. doi:10.1038/ncomms10304

Cho, Y., Song, S. W., Lim, S. Y., Kim, J. H., Park, C. R., and Kim, H. M. (2017). Spectral evidence for multi-pathway contribution to the upconversion pathway in $NaYF_4$:Yb^{3+}, Er^{3+} phosphors. *Phys. Chem. Chem. Phys.* 19, 7326–7332. doi:10.1039/c7cp00048k

Dantelle, G., Reita, V., and Delacour, C. (2021). Luminescent Yb^{3+}, Er^{3+}-doped α-$La(IO_3)_3$ nanocrystals for neuronal network bio-imaging and nanothermometry. *Nanomaterials* 11, 479. doi:10.3390/nano11020479

Debasu, M. L., Oliveira, H., Rocha, J., and Carlos, L. D. (2020). Colloidal $(Gd_{0.98}Nd_{0.02})_2O_3$ nanothermometers operating in a cell culture medium within the first and second biological windows. *J. Rare Earths* 38, 483–491. doi:10.1016/j.jre.2019.12.011

Di, X., Wang, D., Zhou, J., Zhang, L., Stenzel, M. H., Su, Q. P., et al. (2021). Quantitatively monitoring iIn-situ mitochondrial thermal dynamics by upconversion nanoparticles. *Nano Lett.* 21, 1651–1658. doi:10.1021/acs.nanolett.0c04281

Dos Santos, L. F., Martins, J. C., Lima, K. O., Gomes, L. F. T., De Melo, M. T., Tedesco, A. C., et al. (2022). *In-vitro* assays and nanothermometry studies of infrared-to-visible upconversion of nanocrystalline Er^{3+}, Yb^{3+} co-doped Y_2O_3 nanoparticles for theranostic applications. *Phys. B Condens. Matter* 624, 413447. doi:10.1016/j.physb.2021.413447

Dramicanin, M. (2018). *Luminescence thermometry: methods, materials, and applications*. Sawston: Woodhead Publishing.

FDA (2020). Medical lasers - laws, regulations & performance standards. Radiation-Emitting Prod. Proced. Available at: https://www.fda.gov/radiation-emitting-products/surgical-and-therapeutic-products/medical-lasers#lrps.

Freitas, L. F. de, and Hamblin, M. R. (2016). Proposed mechanisms of photobiomodulation or low-level light therapy. *IEEE J. Sel. Top. Quantum Electron.* 22, 348–364. doi:10.1109/JSTQE.2016.2561201

Jaque, D., Martínez Maestro, L., Del Rosal, B., Haro-Gonzalez, P., Benayas, A., Plaza, J. L., et al. (2014). Nanoparticles for photothermal therapies. *Nanoscale* 6, 9494–9530. doi:10.1039/c4nr00708e

Jaque, D., and Vetrone, F. (2012). Luminescence nanothermometry. *Nanoscale* 4, 4301–4326. doi:10.1039/c2nr30764b

Kim, J. S., Lee, S. K., Doh, H., Kim, M. Y., and Kim, D. K. (2021). Real-time tracking of highly luminescent mesoporous silica particles modified with europium β-diketone chelates in living cells. *Nanomaterials* 11, 343–416. doi:10.3390/nano11020343

Kraft, M., Würth, C., Muhr, V., Hirsch, T., and Resch-Genger, U. (2018). Particle-size-dependent upconversion luminescence of $NaYF_4$: Yb, Er nanoparticles in organic solvents and water at different excitation power densities. *Nano Res.* 11, 6360–6374. doi:10.1007/s12274-018-2159-9

Marciniak, L., Szalkowski, M., Bednarkiewicz, A., and Elzbieciak-Piecka, K. (2022). A Cr^{3+} luminescence-based ratiometric optical laser power meter. *J. Mat. Chem. C* 10, 11040–11047. doi:10.1039/D2TC02348B

Martínez, E. D., Brites, C. D. S., Carlos, L. D., García-Flores, A. F., Urbano, R. R., and Rettori, C. (2019). Electrochromic switch devices mixing small- and large-sized upconverting nanocrystals. *Adv. Funct. Mat.* 29, 1807758–1807812. doi:10.1002/adfm.201807758

Martins, J. C., Bastos, A. R. N., Ferreira, R. A. S., Wang, X., Chen, G., and Carlos, L. D. (2021). Primary luminescent nanothermometers for temperature measurements reliability assessment. *Adv. Photonics Res.* 2, 2000169. doi:10.1002/adpr.202000169

Maturi, F. E., Brites, C. D. S., Silva, R. R., Nigoghossian, K., Wilson, D., Ferreira, R. A. S., et al. (2021). Sustainable smart tags with two-step verification for anticounterfeiting triggered by the photothermal response of upconverting nanoparticles. *Adv. Photonics Res.* 3, 2100227. doi:10.1002/adpr.202100227

Mooney, J., and Kambhampati, P. (2013). Get the basics right: Jacobian conversion of wavelength and energy scales for quantitative analysis of emission spectra. *J. Phys. Chem. Lett.* 4, 3316–3318. doi:10.1021/jz401508t

Pini, F., Francés-Soriano, L., Peruffo, N., Barbon, A., Hildebrandt, N., and Natile, M. M. (2022). Spatial and temporal resolution of luminescence quenching in small upconversion nanocrystals. *ACS Appl. Mat. Interfaces* 14, 11883–11894. doi:10.1021/acsami.1c23498

Piñol, R., Zeler, J., Brites, C. D. S., Gu, Y., Téllez, P., Carneiro Neto, A. N., et al. (2020). Real-time intracellular temperature imaging using lanthanide-bearing polymeric micelles. *Nano Lett.* 20, 6466–6472. doi:10.1021/acs.nanolett.0c02163

Ramalho, J. F. C. B., Dias, L. M. S., Fu, L., Botas, A. M. P., Carlos, L. D., Carneiro Neto, A. N., et al. (2021). Customized luminescent multiplexed quick-response codes as reliable temperature mobile optical sensors for eHealth and internet of things. *Adv. Photonics Res.* 3, 2100206. doi:10.1002/adpr.202100206

Renero-Lecuna, C., Martín-Rodríguez, R., Valiente, R., González, J., Rodríguez, F., Krämer, K. W., et al. (2011). Origin of the high upconversion green luminescence efficiency in β-$NaYF_4$: 2%Er^{3+}, 20%Yb^{3+}. *Chem. Mat.* 23, 3442–3448. doi:10.1021/cm2004227

Rühl, P., Wang, D., Garwe, F., Müller, R., Haase, M., Krämer, K. W., et al. (2021). Notes on thermometric artefacts by Er^{3+} luminescence band interference. *J. Lumin.* 232, 117860–117921. doi:10.1016/j.jlumin.2020.117860

Shen, Y., Santos, H. D. A., Ximendes, E. C., Lifante, J., Sanz-Portilla, A., Monge, L., et al. (2020). Ag_2S nanoheaters with multiparameter sensing for reliable thermal feedback during *in vivo* tumor therapy. *Adv. Funct. Mat.* 30, 2002730–2002813. doi:10.1002/adfm.202002730

Shi, R., Brites, C. D. S., and Carlos, L. D. (2022). Understanding the shell passivation in ln^{3+}-doped luminescent nanocrystals. *Small Struct.* 3, 2100194. doi:10.1002/sstr.202100194

Skripka, A., Benayas, A., Brites, C. D. S., Martín, I. R., Carlos, L. D., and Vetrone, F. (2020). Inert shell effect on the quantum yield of neodymium-doped near-infrared nanoparticles: The necessary shield in an aqueous dispersion. *Nano Lett.* 20, 7648–7654. doi:10.1021/acs.nanolett.0c03187

Van Swieten, T. P., Meijerink, A., and Rabouw, F. T. (2022). Impact of noise and background on measurement uncertainties in luminescence thermometry. *ACS Photonics* 9, 1366–1374. doi:10.1021/acsphotonics.2c00039

Van Swieten, T. P., Van Omme, T., Van Den Heuvel, D. J., Vonk, S. J. W., Spruit, R. G., Meirer, F., et al. (2021). Mapping elevated temperatures with a micrometer resolution using the luminescence of chemically stable upconversion nanoparticles. *ACS Appl. Nano Mat.* 4, 4208–4215. doi:10.1021/acsanm.1c00657

Vetrone, F., Naccache, R., Zamarrón, A., De La Fuente, A. J., Sanz-Rodríguez, F., Maestro, L. M., et al. (2010). Temperature sensing using fluorescent nanothermometers. *ACS Nano* 4, 3254–3258. doi:10.1021/nn100244a

Wang, J., and Dong, J. (2020). Optical waveguides and integrated optical devices for medical diagnosis, health monitoring and light therapies. *Sensors* 20, 3981. doi:10.3390/s20143981

Wang, Y. (2019). The role of an inert shell in improving energy utilization in lanthanide-doped upconversion nanoparticles. *Nanoscale* 11, 10852–10858. doi:10.1039/C9NR03205C

Xia, X., Volpi, A., Roh, J. Y. D., De Siena, M. C., Gamelin, D. R., Hehlen, M. P., et al. (2021). The impact of $^2H_{9/2} \rightarrow {}^4I_{13/2}$ emission from Er^{3+} ions on ratiometric optical temperature sensing with Yb^{3+}/Er^{3+} Co-doped upconversion materials. *J. Lumin.* 236, 118006. doi:10.1016/j.jlumin.2021.118006

Yang, T. D., Park, K., Kim, H.-J., Im, N.-R., Kim, B., Kim, T., et al. (2017). *In-vivo* photothermal treatment with real-time monitoring by optical fiber-needle array. *Biomed. Opt. Express* 8, 3482. doi:10.1364/boe.8.003482

Yuan, M., Wang, R., Zhang, C., Yang, Z., Cui, W., Yang, X., et al. (2018). Exploiting the silent upconversion emissions from a single β-$NaYF_4$:Yb/Er microcrystal via saturated excitation. *J. Mat. Chem. C* 6, 10226–10232. doi:10.1039/c8tc02193g

Yuan, M., Wang, R., Zhang, C., Yang, Z., Yang, X., Han, K., et al. (2019). Revisiting the enhanced red upconversion emission from a single β-$NaYF_4$:Yb/Er microcrystal by doping with Mn^{2+} ions. *Nanoscale Res. Lett.* 14, 103. doi:10.1186/s11671-019-2931-0

Zhou, J., Liu, Q., Feng, W., Sun, Y., and Li, F. (2015). Upconversion luminescent materials: Advances and applications. *Chem. Rev.* 115, 395–465. doi:10.1021/cr400478f

Zhou, S., Deng, K., Wei, X., Jiang, G., Duan, C., Chen, Y., et al. (2013). Upconversion luminescence of $NaYF_4$: Yb^{3+}, Er^{3+} for temperature sensing. *Opt. Commun.* 291, 138–142. doi:10.1016/j.optcom.2012.11.005

Zhu, X., Feng, W., Chang, J., Tan, Y. W., Li, J., Chen, M., et al. (2016). Temperature-feedback upconversion nanocomposite for accurate photothermal therapy at facile temperature. *Nat. Commun.* 7, 10437. doi:10.1038/ncomms10437

Zhu, X., Li, J., Qiu, X., Liu, Y., Feng, W., and Li, F. (2018). Upconversion nanocomposite for programming combination cancer therapy by precise control of microscopic temperature. *Nat. Commun.* 9, 2176. doi:10.1038/s41467-018-04571-4

Ziegelberger, G. (2013). ICNIRP guidelines on limits of exposure to laser radiation of wavelengths between 180 nm and 1, 000 μm. *Health Phys.* 105, 271–295. doi:10.1097/HP.0b013e3182983fd4